Supplementary Information for

An off-the-shelf light-sheet microscopy ecosystem enables versatile cleared-tissue imaging across scales and applications

Yuki Nozawa†, Steven Edwards†, Kiyotada Naitou†, *, Maximilian Senftleben†, Akira L. Yoshikawa, Yukihiko Sato, Yuri Saito, Yuichi Wada,Takenobu Nii, Chikara Meno, Kohei Otomo, Hjalmar Brismar*, and Etsuo A. Susaki*

†Co-first authors

*Corresponding to

Kiyotaka Naitou（k6845196@kadai.jp）

Hjalmar Brismar（hjalmar.brismar@scilifelab.se）

Etsuo A. Susaki (suishess-kyu@umin.ac.jp)

This PDF file includes:

Supplementary Figs. 1 to 13

Supplementary Table 1

Supplementary References

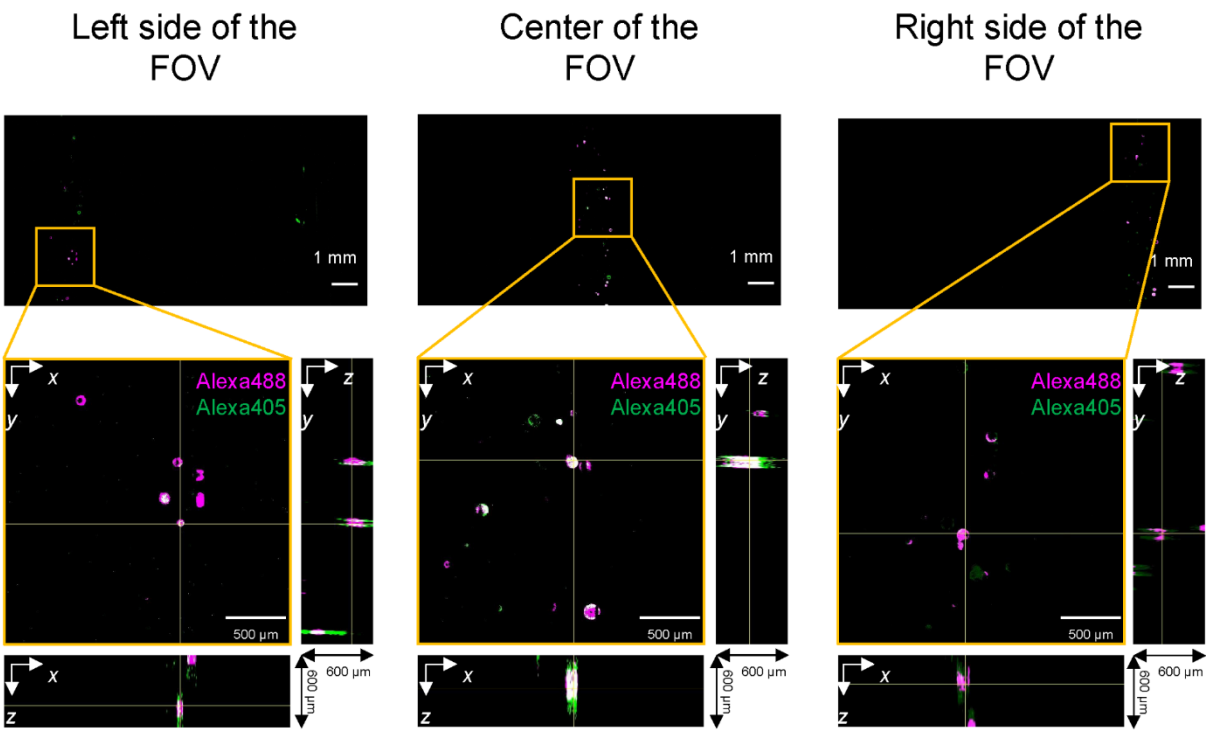

Supplementary Fig. 1 | Alignment of two single-mode fiber outputs merged via a polarizing beam splitter

This figure shows imaging data before and after alignment of two single-mode fiber laser outputs (Cobolt Skyra: 488 nm/50 mW, 561 nm/50 mW, 647 nm/50 mW; Cobolt C-FLEX: 405 nm/50 mW, 730 nm/50 mW) merged into a single excitation path via a polarizing beam splitter. To assess alignment performance, a dual-color optical phantom was prepared by conjugating Alexa Fluor® 405 and Alexa Fluor® 488 (equal amounts) to Protein A/G PLUS-Agarose beads and embedding them in 1% PBS–agarose gel. Imaging was performed with 405 nm and 488 nm excitation, where Alexa Fluor® 405 is shown in green and Alexa Fluor® 488 in magenta. The excitation power and exposure time were set to 1 mW and 50 ms for 405 nm, and 5 mW and 100 ms for 488 nm, respectively. A manual translator (CXY1A, Thorlabs) was placed on the single-mode fiber side of the polarizing beam splitter for the Cobolt C-FLEX 405 nm line. Fluorescence was directed to a CMOS camera via a kinematic cage cube with a removable silver mirror (mirror inserted). Stacked images were acquired over 30 steps with 20 µm intervals, covering a total range of 600 µm. Alignment was evaluated in XY, XZ, and YZ planes. Imaging was performed using the automated workflow described in **Supplementary Fig. 12**.

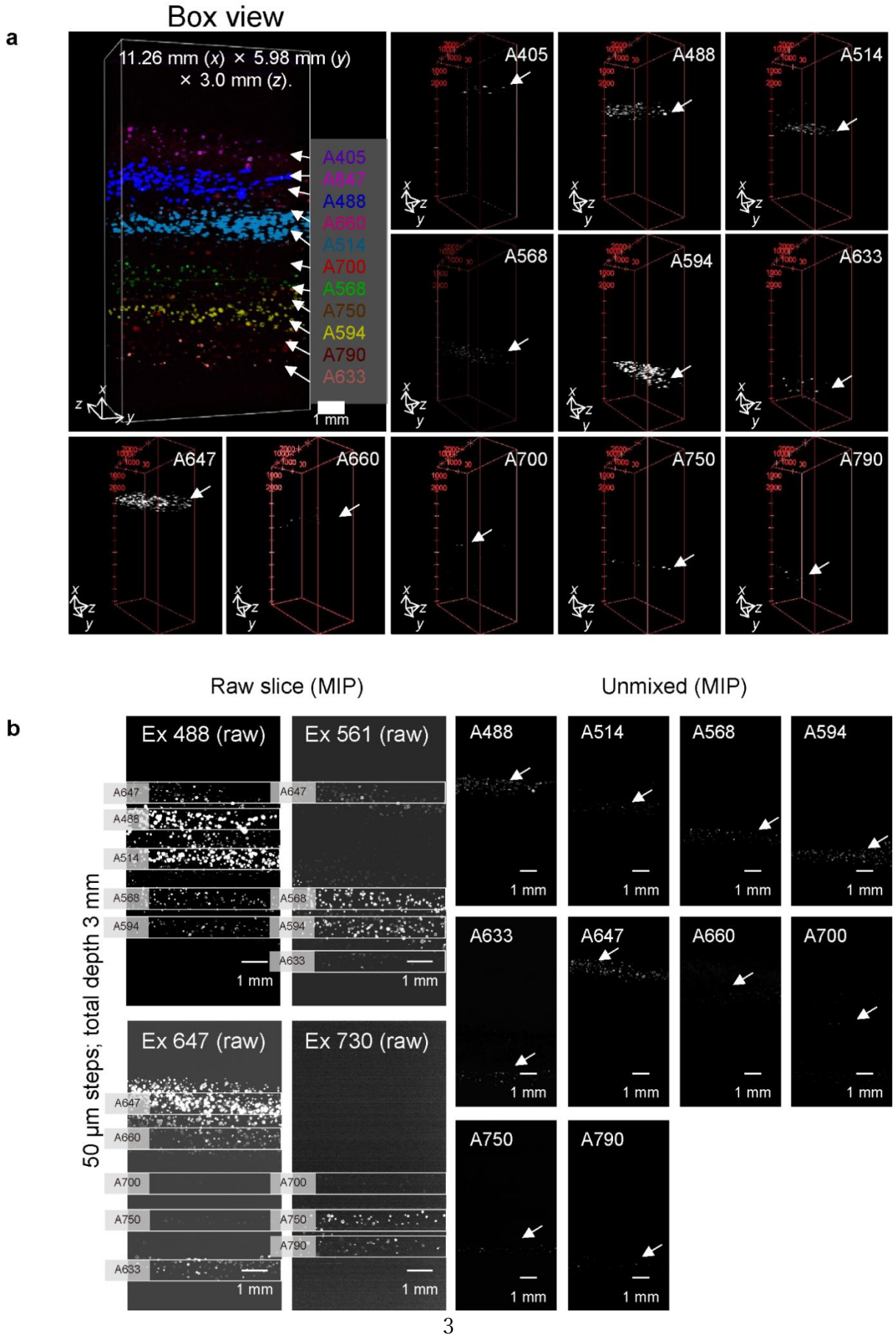
a
Box view
11.26 mm (x) × 5.98 mm (y) × 3.0 mm (z).
A405
A647
A488
A660
A514
A700
A568
A750
A594
A790
A633
1 mm
A405
A488
A514
A568
A594
A633
A647
A660
A700
A750
A790
b
Raw slice (MIP)
Unmixed (MIP)
Ex 488 (raw)
Ex 561 (raw)
Ex 647 (raw)
Ex 730 (raw)
50 µm steps; total depth 3 mm
1 mm

Supplementary Fig. 2 | Multiplexed fluorescence imaging of an optical phantom composed of Protein A/G agarose beads labeled with Alexa Fluor® dyes.

a, Three-dimensional rendering of a 60-slice hyperspectral dataset acquired from a structured optical phantom, together with corresponding 3D renderings of the individual fluorescence channels. The phantom was composed of Protein A/G PLUS–agarose beads, each conjugated with a fluorescent secondary antibody carrying a single Alexa Fluor® dye. The beads were embedded in 1% PBS–agarose and arranged in layers within a four-sided transmission cuvette. The sample was imaged using descSPIM-Galaxy with five excitation lines (405, 488, 561, 647, and 730 nm) and a hyperspectral detector covering 470–900 nm with up to 150 spectral channels. The acquired volume was 5.98 mm × 11.26 mm × 3.00 mm (x × y × z), consisting of 60 slices acquired at 50 µm intervals. Laser power was set to 100 mW for 405 nm excitation and 50 mW for all other excitation wavelengths, with an exposure time of 300 ms per frame. For each excitation wavelength, only emission above the cutoff wavelength of the corresponding long-pass filter was analyzed. Single-color bead spectra were used as endmembers for linear spectral unmixing by non-negative least squares (NNLS) of the 488, 561, 647, and 730 nm excitation datasets[1], enabling separation of 11 spectrally overlapping fluorophores. The total acquisition time was approximately 15.5 h. The 405 nm excitation dataset was processed without spectral unmixing. For each z-slice, the first three short-wavelength spectral bands were averaged, and the background was subtracted using a morphological opening with a 15-pixel structuring element. The resulting images were thresholded at $T = \mu + 3\sigma$, where μ and σ were calculated from the global mean and standard deviation across all 60 slices, with a fixed multiplier of 3.0. The binary mask was further refined by morphological opening, hole filling, and removal of regions smaller than 10 pixels, and was then applied to 16-bit-scaled images normalized to the global maximum. For Alexa Fluor® 700, the unmixed stack was corrected slice by slice by subtracting the mean raw spectral signal measured at 671.8–674.0 nm, followed by lower clipping at the measured background level and conversion to 8-bit data. **b,** Maximum-intensity projections of the 60-slice stack. Linear spectral unmixing by NNLS was applied to the 488, 561, 647, and 730 nm excitation datasets, and the resulting unmixed images are shown on the right alongside the corresponding raw images on the left. Alexa Fluor® 405 is not shown because the 405 nm excitation dataset was processed without spectral unmixing. For fluorophores efficiently excited by more than one wavelength, such as Alexa Fluor® 568 under both 488 and 561 nm excitation, single-color reference spectra were acquired separately for each excitation wavelength, and spectral

unmixing was performed independently for each dataset. In the final composite image, the excitation channel providing the higher spectral-separation fidelity was selected for each fluorophore.

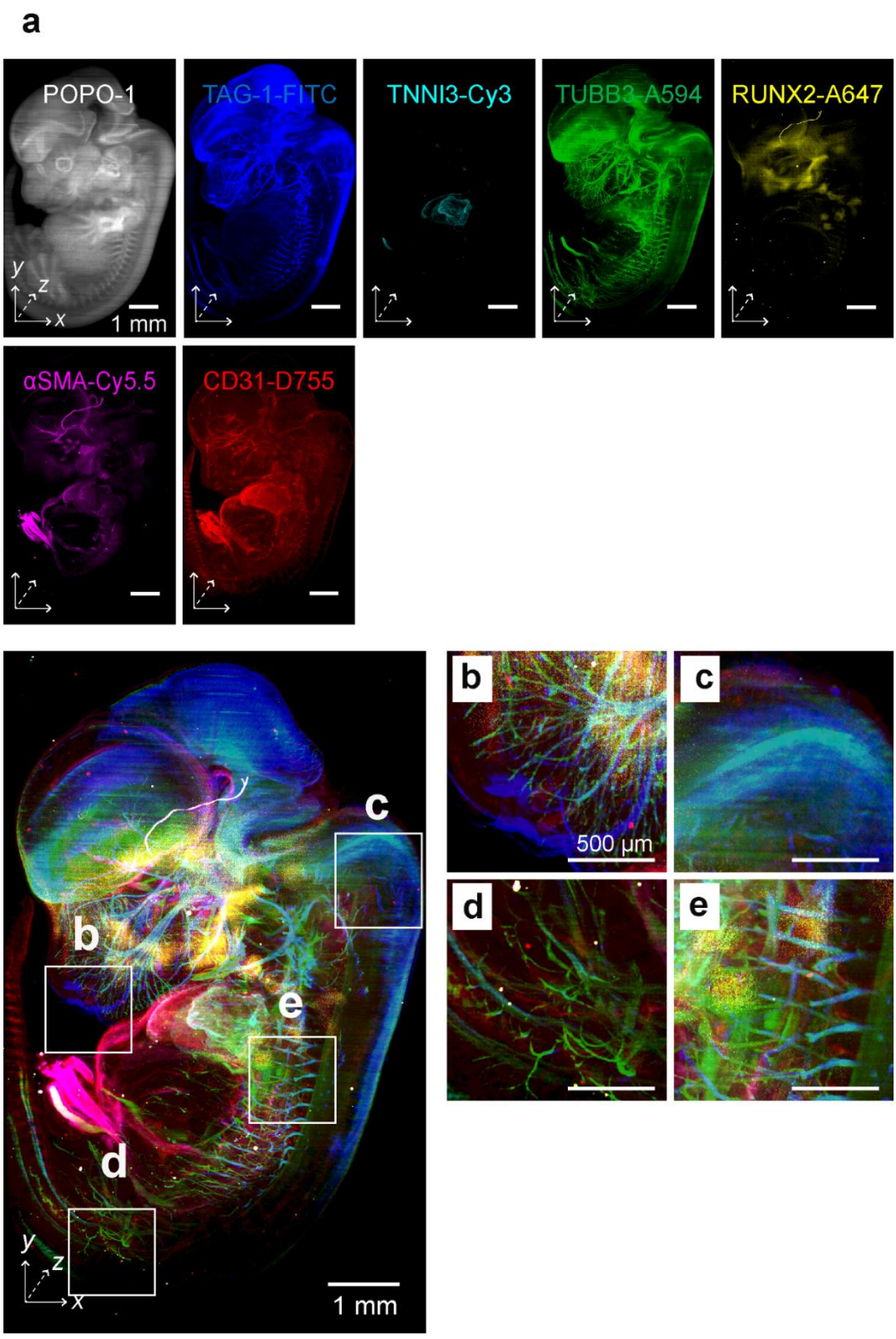

Supplementary Fig. 3 | Enlarged views and single-channel control images of the 7-color whole-embryo dataset.

a, Maximum-intensity projections of single-channel views from the 7-color dataset acquired from a cleared whole E12.5 mouse embryo, showing POPO®-1, TAG1-FITC, TNNI3-Cy3, TUBB3-AF594, RUNX2-AF647, αSMA-Cy5.5, and CD31-DL755. **b–e,** Enlarged views of representative regions of interest selected from the merged 7-color whole-embryo dataset. Scale bars, 1 mm in a; 500 μm in b–e.

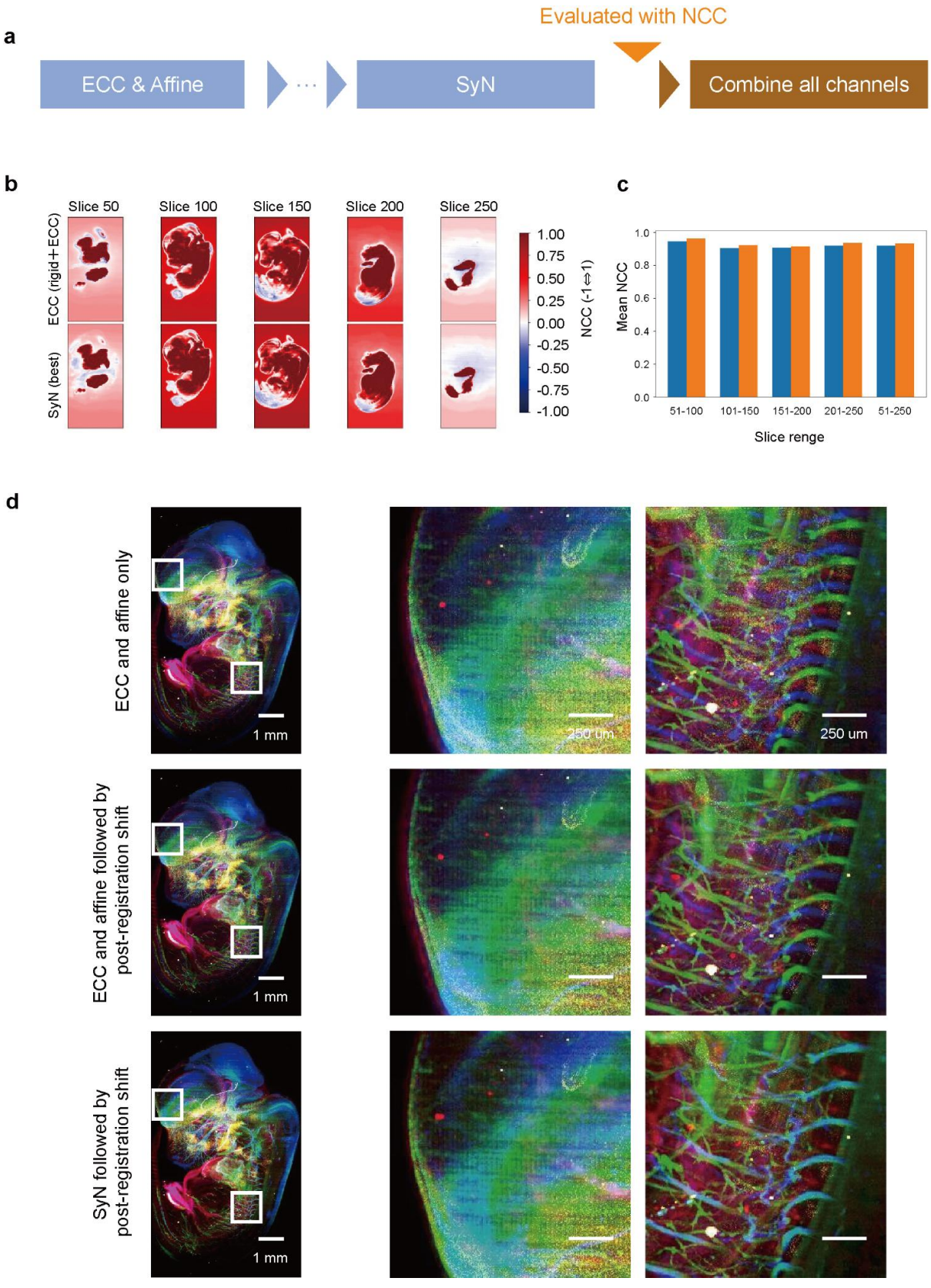
a
Evaluated with NCC
ECC & Affine
SyN
Combine all channels
b
Slice 50
Slice 100
Slice 150
Slice 200
Slice 250
ECC (rigid+ECC)
SyN (best)
1.00
0.75
0.50
0.25
0.00
-0.25
-0.50
-0.75
-1.00
NCC (-1⇔1)
c
Mean NCC
1.0
0.8
0.6
0.4
0.2
0.0
51-100
101-150
151-200
201-250
51-250
Slice renge
d
ECC and affine only
ECC and affine followed by post-registration shift
SyN followed by post-registration shift
1 mm
250 um

Supplementary Fig. 4 | Quantitative and visual evaluation of cross-modal registration performance

a, Schematic illustration of the normalized cross-correlation (NCC) mapping procedure. Following SyN-based nonlinear registration, the nuclear-staining channel (POPO®-1) acquired from a cleared whole E12.5 mouse embryo using the hyperspectral camera was used as the fixed reference image. The corresponding region was acquired using the CMOS camera at the same sample position and with the same step size, producing a 300-slice z-stack. Local NCC maps were then calculated between the two modalities using custom-written code based on the normalized cross-correlation formulation[2,3]. The resulting maps were used to visualize and quantify local image similarity after registration. **b,** Representative NCC maps obtained using different SyN parameter sets. Multiple parameter combinations were evaluated, and the parameter set yielding the highest NCC was selected for subsequent analyses. **c,** Quantitative comparison of NCC values obtained under two registration conditions. Blue, rigid registration with ECC only; orange, ECC followed by SyN using the selected parameter set. NCC values were evaluated across four subranges of the embryo z-stack—slices 51–100, 101–150, 151–200, and 201–250—as well as across the entire region encompassing the embryo, comprising slices 51–250. ECC followed by SyN yielded higher NCC values than ECC only in all evaluated ranges. Across slices 51–250, the mean NCC values were 0.9345 for ECC followed by SyN and 0.9201 for ECC only. **d,** Representative 7-color merged images generated under three registration conditions: ECC and affine registration only, ECC and affine registration followed by post-registration shift correction, and SyN registration followed by post-registration shift correction. The post-registration shift-correction procedure is described in **Supplementary Fig. 5**.

e, ROI-based comparison of two representative locations across the three merged datasets. Residual misalignments remain visible after ECC and affine registration, both with and without post-registration shift correction. By contrast, SyN registration followed by post-registration shift correction improves the alignment of fine structures.

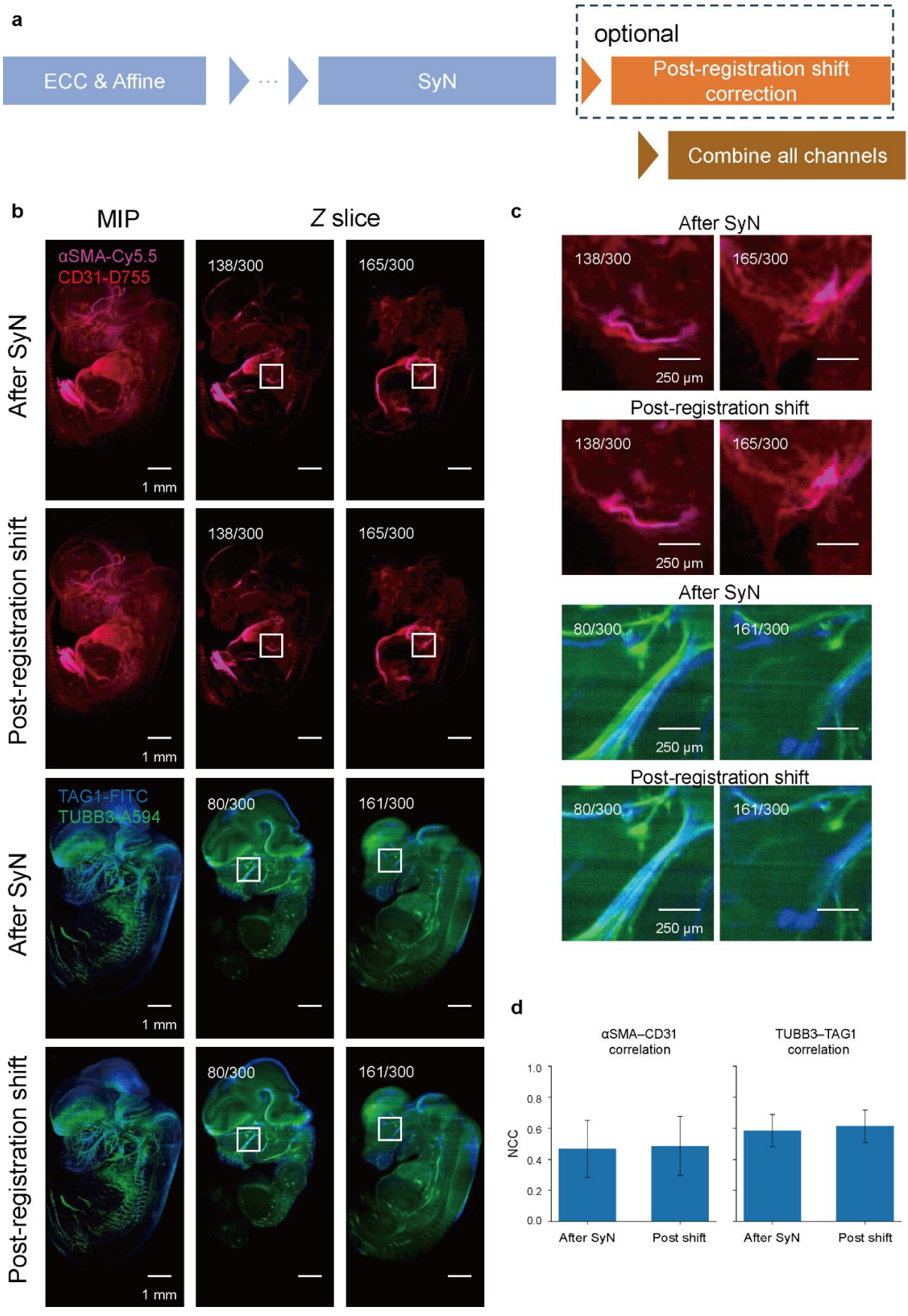
a
ECC & Affine
SyN
optional
Post-registration shift correction
Combine all channels
b
MIP
Z slice
After SyN
Post-registration shift
αSMA-Cy5.5
CD31-D755
TAG1-FITC
TUBB3-A594
138/300
165/300
80/300
161/300
1 mm
c
After SyN
Post-registration shift
250 μm
d
αSMA–CD31 correlation
TUBB3–TAG1 correlation
NCC
1.0
0.8
0.6
0.4
0.2
0.0
After SyN
Post shift

Supplementary Fig. 5 | Linear post-registration correction shift of residual misalignment by in-plane (x–y) shift.

a, Schematic illustration of post-registration shift correction following SyN-based nonlinear registration. **b,** Maximum-intensity projections (MIPs) and representative z-slices comparing images before shift correction (after SyN registration alone) and after post-registration shift correction for two marker pairs: αSMA–CD31 (top) and TUBB3–TAG1 (bottom). **c,** Magnified views of selected regions of interest highlighting residual misalignments corrected by the linear in-plane shift. **d,** Slice-wise comparison of normalized cross-correlation (NCC) values across slices 51–250 before and after post-registration shift correction for the αSMA–CD31 and TUBB3–TAG1 channel pairs. Bars show the mean NCC, and error bars indicate the standard deviation across the 200 evaluated slices. Post-registration shift correction increased the mean NCC from 0.467 to 0.486 for αSMA–CD31 and from 0.586 to 0.613 for TUBB3–TAG1.

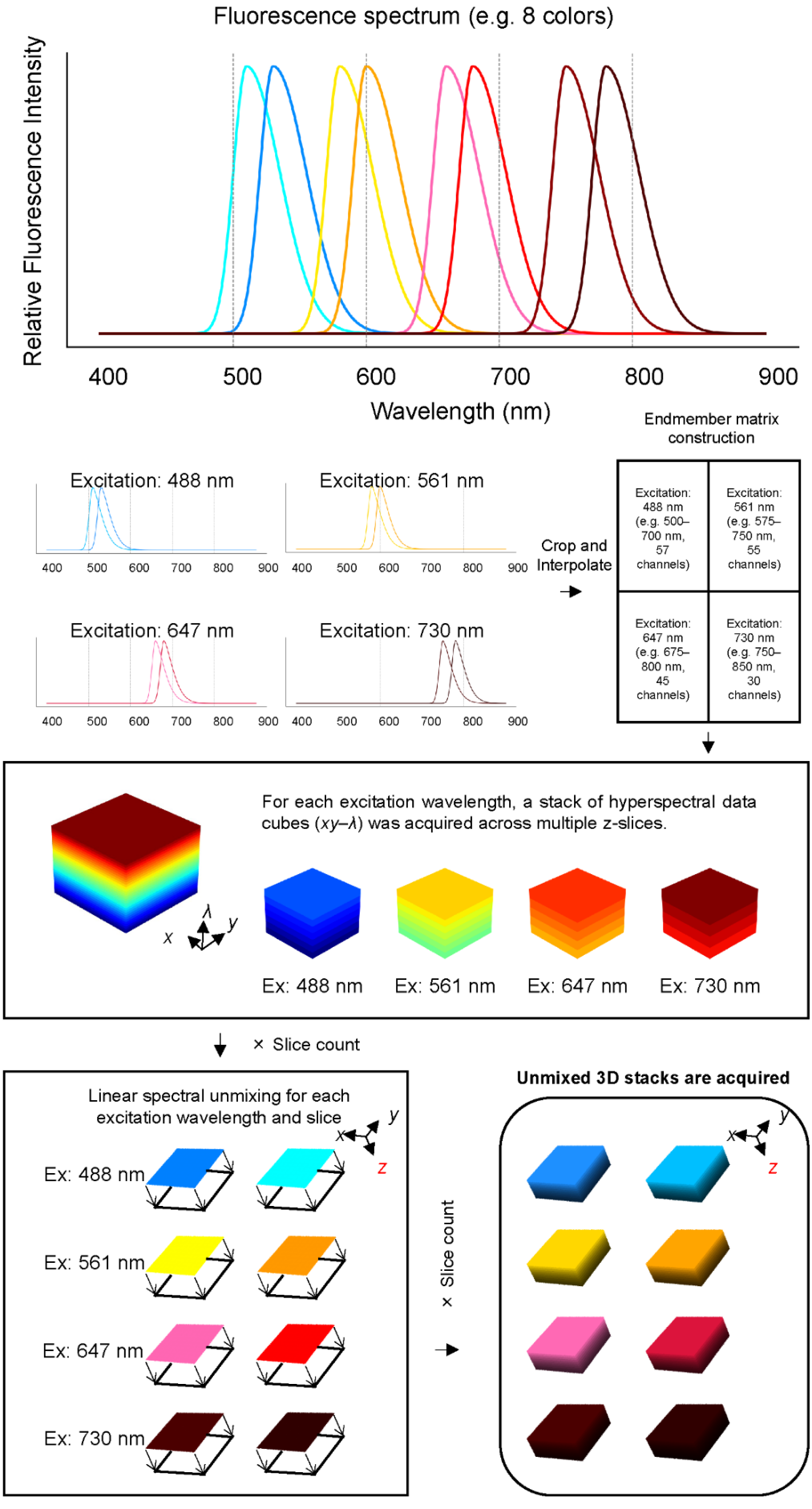
Fluorescence spectrum (e.g. 8 colors)
Relative Fluorescence Intensity
400
500
600
700
800
900
Wavelength (nm)
Endmember matrix construction
Excitation: 488 nm
Excitation: 561 nm
Excitation: 647 nm
Excitation: 730 nm
Crop and Interpolate
Excitation: 488 nm (e.g. 500–700 nm, 57 channels)
Excitation: 561 nm (e.g. 575–750 nm, 55 channels)
Excitation: 647 nm (e.g. 675–800 nm, 45 channels)
Excitation: 730 nm (e.g. 750–850 nm, 30 channels)
For each excitation wavelength, a stack of hyperspectral data cubes (xy–λ) was acquired across multiple z-slices.
Ex: 488 nm
Ex: 561 nm
Ex: 647 nm
Ex: 730 nm
× Slice count
Linear spectral unmixing for each excitation wavelength and slice
Ex: 488 nm
Ex: 561 nm
Ex: 647 nm
Ex: 730 nm
× Slice count
Unmixed 3D stacks are acquired

Supplementary Fig. 6 | Workflow for fluorescence separation using linear unmixing applied to hyperspectral 3D imaging data.

Single-stained reference samples were prepared for each fluorophore under the same imaging conditions and in the same embedding buffer as the multiplexed specimen. Fluorescence spectra were recorded for each excitation wavelength that elicited measurable emission, and dyes excited by multiple wavelengths were characterized separately for each excitation condition. Spectral channels below the relevant long-pass cutoff were excluded, and the remaining valid spectral bands were used for subsequent analysis. Averaging a broad region of interest yielded low-noise endmember spectra, which were exported as CSV files from the hyperspectral-camera GUI, cropped to the relevant wavelength range, and interpolated onto the spectral grid to form the endmember matrix.

Linear unmixing was then performed slice-by-slice along the z-stack using a NNLS algorithm[1], selected for its balance of speed and numerical stability. Processing time increased approximately linearly with the number of slices because a single endmember set was reused for all slices. The unmixed images were saved in TIFF format to preserve quantitative precision, and the planes belonging to each fluorophore were concatenated into a multipage TIFF stack representing its three-dimensional distribution. The entire procedure was implemented in a dedicated Python GUI application.

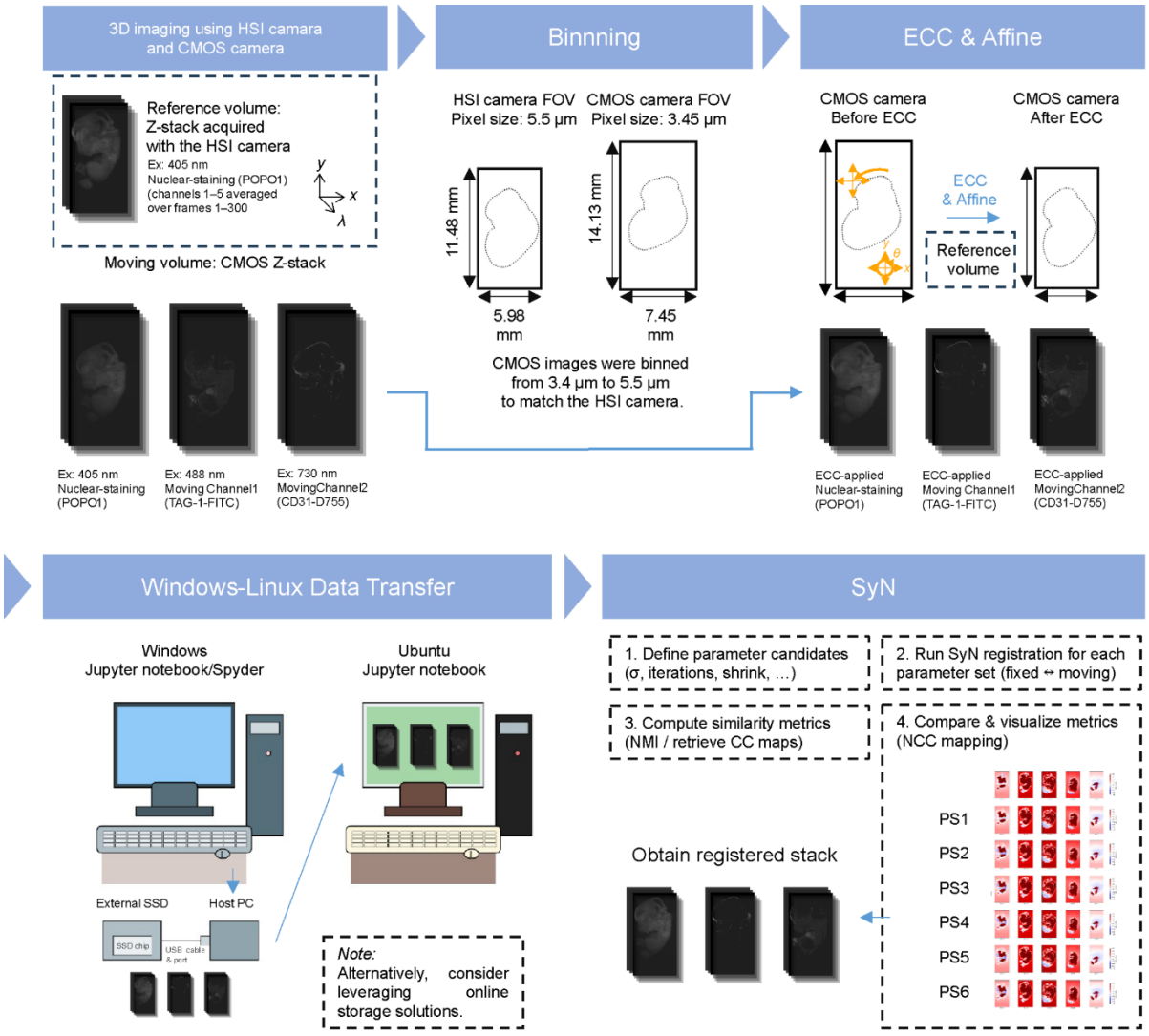

Supplementary Fig. 7 | Image registration workflow between hyperspectral and CMOS camera data.

A hyperspectral camera and a CMOS camera acquire multi-slice images from the same light-sheet plane. The CMOS camera records one fluorescence stack for each excitation wavelength without linear unmixing, whereas the hyperspectral data are linearly unmixed to generate individual fluorescence stacks for each fluorophore. Because the two cameras have different fields of view and effective pixel sizes (CMOS, 3.45 µm per pixel; hyperspectral, 5.5 µm per pixel), the CMOS images are downsampled to 5.5 µm per pixel. After matching the pixel sizes, an in-plane Euclidean transformation, accounting for translation and rotation, is estimated using the Enhanced Correlation Coefficient (ECC) algorithm from maximum-intensity projections and applied to each slice of the CMOS stacks, bringing them into the field of view of the hyperspectral stacks. The images are subsequently subjected to nonlinear

registration using Symmetric Normalization (SyN)[2,3,4]. An exhaustive parameter-grid search is performed, and the SyN settings that maximize normalized cross-correlation between the two modalities are selected.

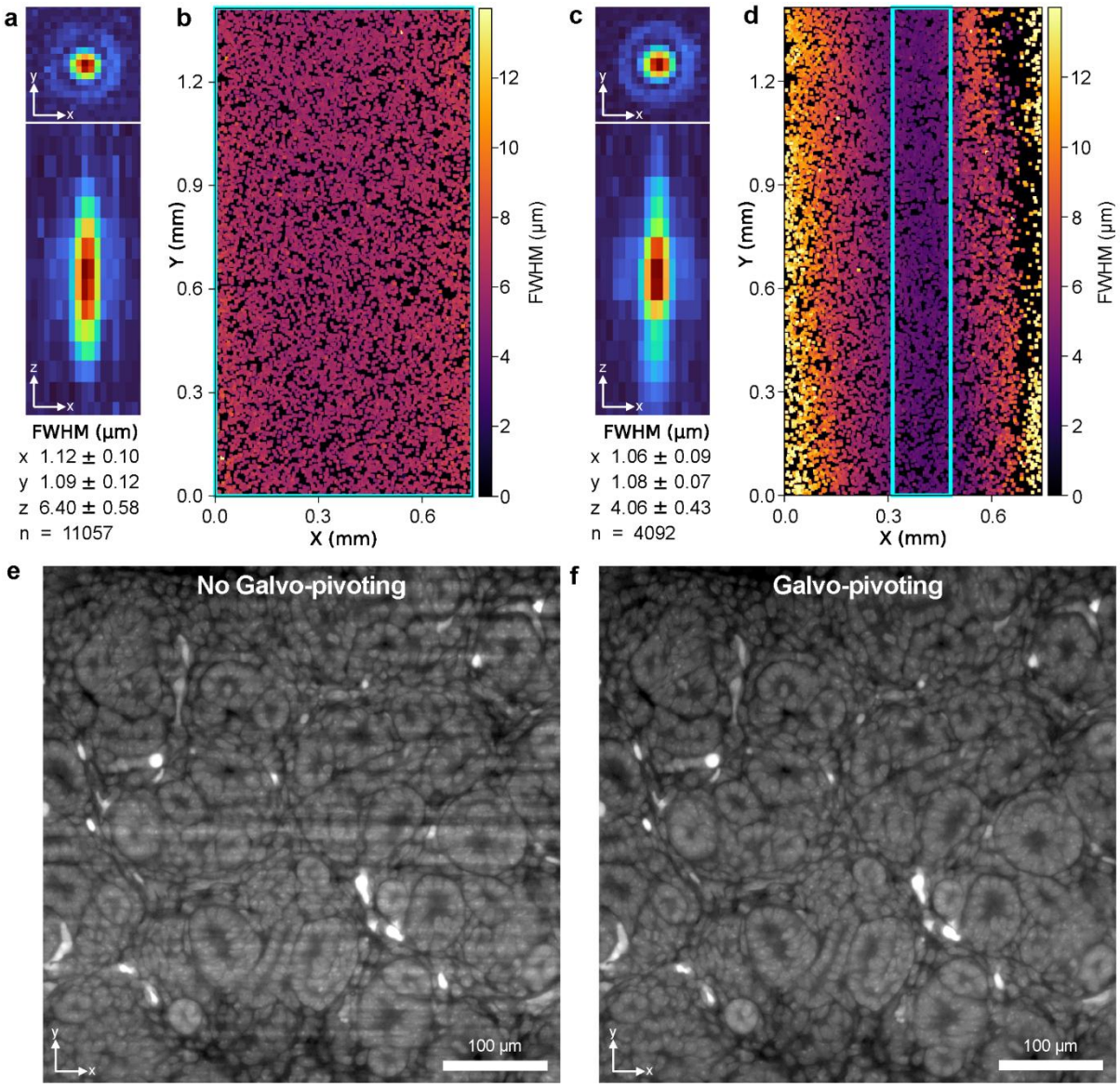

Supplementary Fig. 8 | Performance of descSPIM-Deepsky.

a, Representative PSF of a single bead imaged with a thick light-sheet. The upper diagram shows the xy-plane while the lower diagram shows the zx-plane. The resolution was measured to be around 1.10 µm laterally and 6.40 µm axially on average. **b,** Axial full-width-half-maximum (FWHM) representation shows a homogenous light-sheet waist for the thick light-sheet over the entire FOV. **c,** Similarly, FWHM measurements for the thin light-sheet with lateral resolution of 1.07 µm and axial resolution of 4.06 µm. (d) Similar axial FWHM representation for the thin light-sheet shows that only 22.7 % of the FWHM around the center

can be used for imaging. However, the thin light-sheet renders a higher axial resolution. The beam waist was measured to be w0 = 3.78 µm by measuring a representative bead in the center of the FOV. (e, f) Light-sheet-pivoting in descSPIM Deepsky removes shadowing artifacts in cleared rat embryonic kidney.

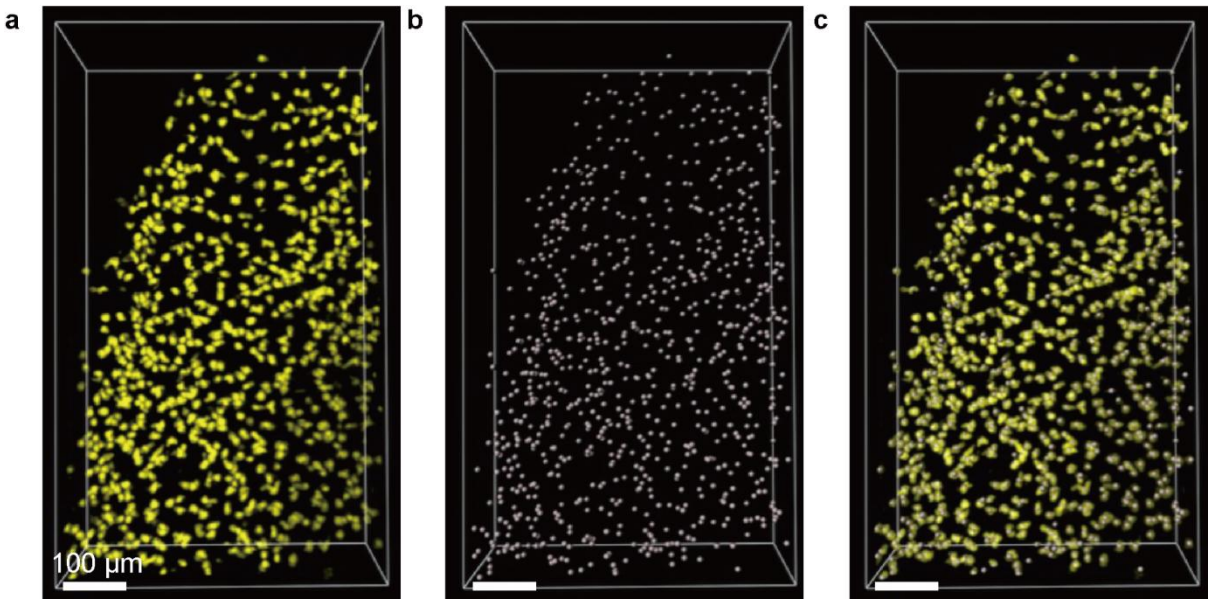

Supplementary Fig. 9 | Counting of GFP-positive type II in cleared mouse lung.

a, 3D render of GFP expressing type II cells **b,** spatial distribution of detected cells using automated spot detection in Imaris 11.0.1 **c**, 3D render overlaid with detected cells using automated spot detection. Scale bars = 100 µm

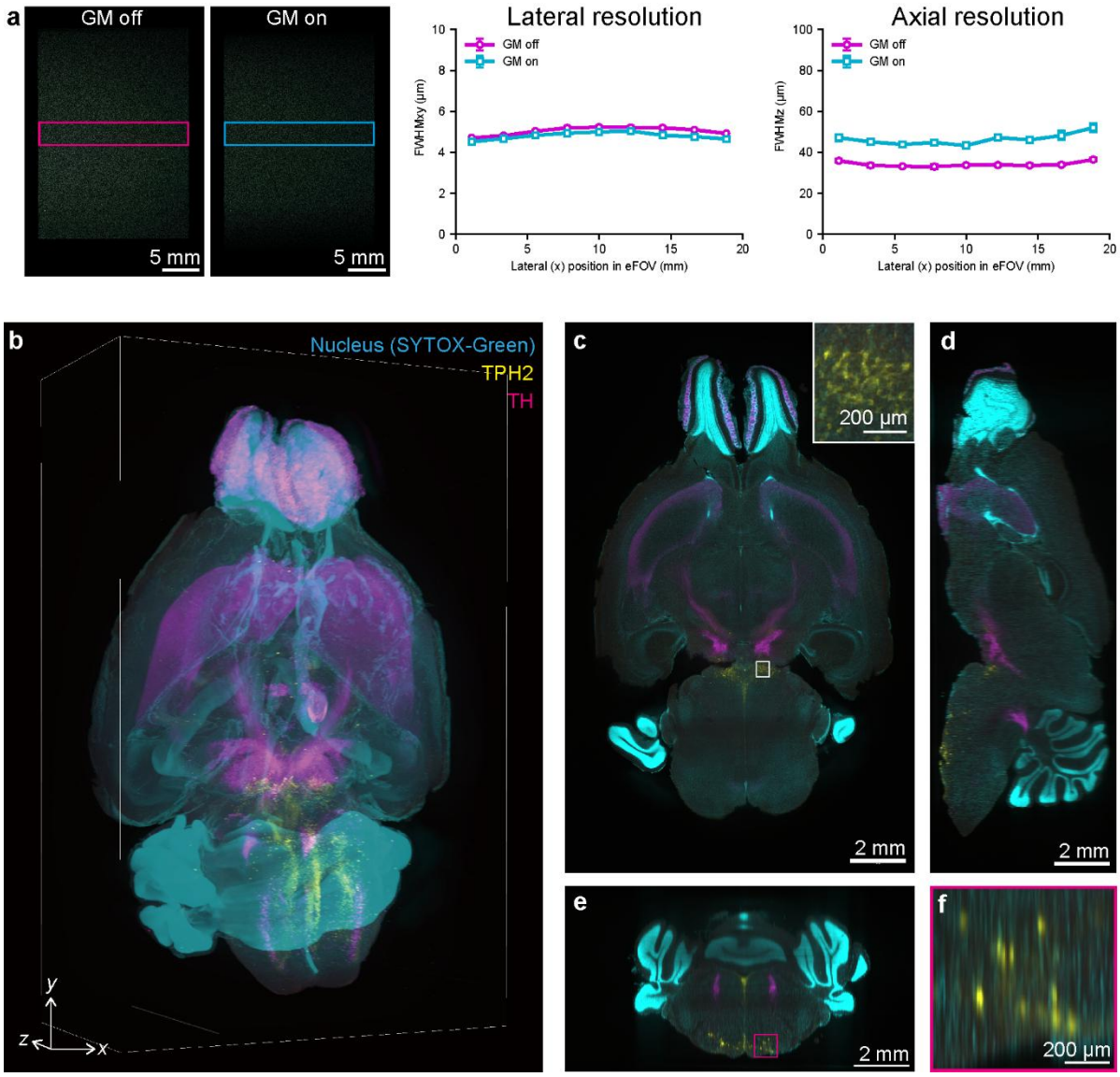

Supplementary Fig. 10 | Optical characterization and representative imaging data and optical section images of descSPIM-Fullmoon

a, Representative eFOV images and lateral-position-dependent PSF plots. Images are maximum-intensity projections generated from a 100-µm z stack of Φ1 µm fluorescent beads distributed throughout a 20-mm-wide glass cuvette and imaged with descSPIM-Fullmoon over the entire camera sensor (23.8 mm × 35.8 mm), with the galvanometer mirror (GM) turned off (left) or on (right). When a 20-mm-wide cuvette was used, the eFOV was limited to 19.8 mm × 28.1 mm. The eFOV was defined as the range over which fluorescence from the beads was detected in the average line intensity profile of the image acquired without light-sheet pivoting. Light-sheet pivoting slightly reduced fluorescence intensity at the upper and lower edges of the eFOV. Plots show lateral-position-dependent PSF variations across the eFOV,

measured within the boxed regions in the images. Magenta and cyan indicate GM off and GM on, respectively. The boxed region was divided into nine equal sections, and the central 200 × 200 pixel area of each section was analyzed. For each section, the mean ± s.d. of FWHM was calculated (n = 10). Lateral FWHMxy (left) and axial FWHMz (right) are shown. Light-sheet pivoting did not affect the lateral FWHMxy but increased the axial FWHMz. **b,** Three-dimensional reconstruction of a CUBIC-X-expanded mouse whole brain. Cyan, nuclei (SYTOX® Green); yellow, tryptophan hydroxylase 2 (Tph2); magenta, tyrosine hydroxylase (Th). **c–f,** Representative single optical sections from the sample shown in d, corresponding to the xy (e, inset: a magnified view of the boxed region), reconstructed yz plane (f), reconstructed xz plane (g), and magnified view of the boxed region in g (h).

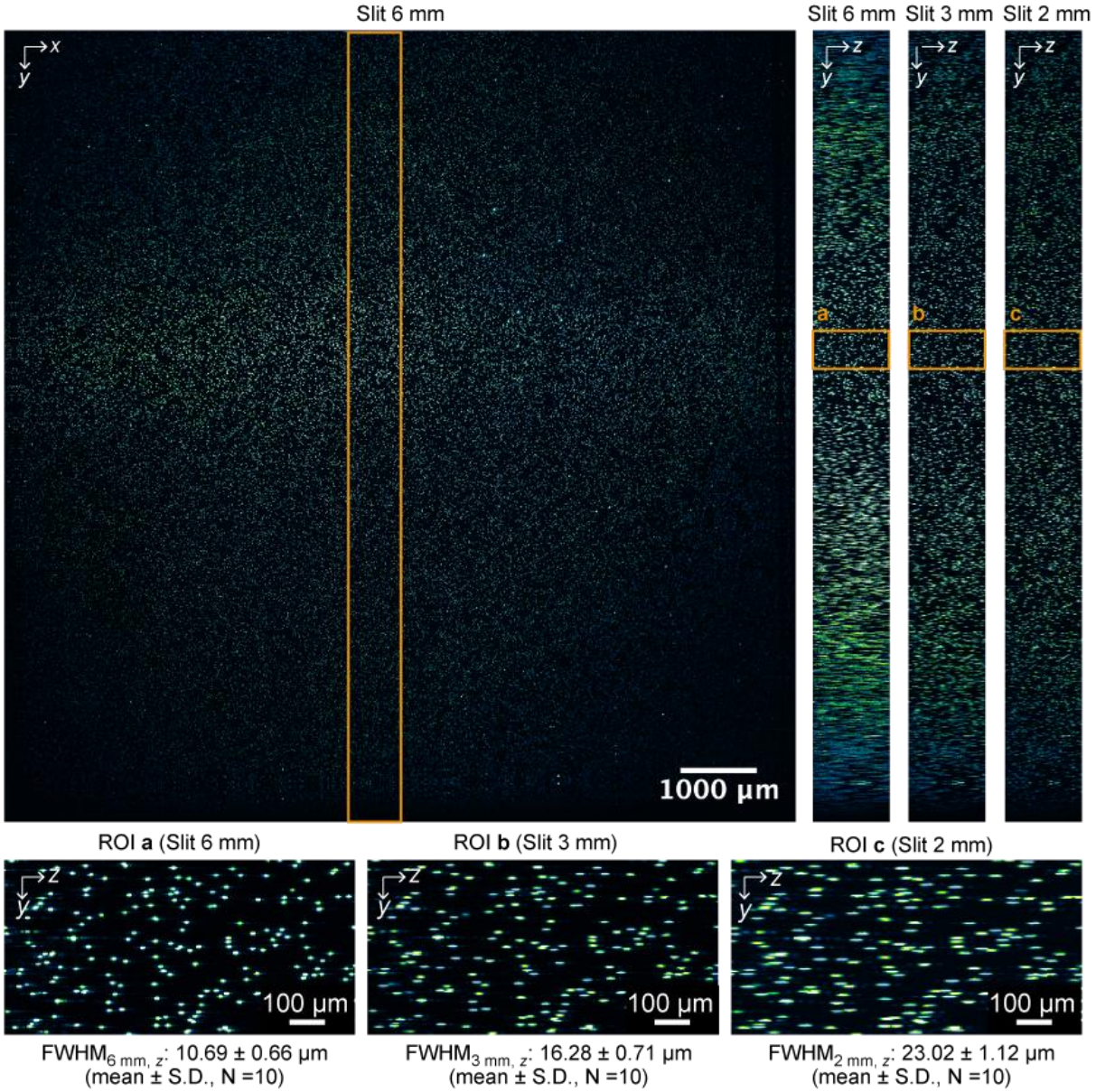

Supplementary Fig. 11 | Point-spread function analysis of descSPIM-SLIM using a fiber-coupled laser light source.

Representative images of 1-µm fluorescent beads acquired with descSPIM-SLIM using a single-mode-fiber-coupled laser light source. The left panel shows an xy maximum-intensity projection, with the orange rectangle indicating the region used for yz cross-sectional analysis. The three vertical panels on the right show yz views obtained with slit widths of 6 mm, 3 mm and 2 mm. Orange boxes indicate the regions enlarged in the bottom panels. The slit was placed after beam collimation and before the cylindrical lens to tune the effective excitation

numerical aperture and light-sheet thickness. At narrower slit settings, the broadened light sheet increased the effective illumination coverage within the camera field of view, enabling a larger usable imaging field at the expense of axial confinement. Compared with the standard compact laser-diode-module configuration described in Fig. 4, the fiber-coupled laser-light-source configuration showed a broader axial point-spread function, even at the same 6-mm slit setting. This difference is likely attributable to differences in the illumination beam profile: in the fiber-coupled configuration, the single-mode-fiber output was directly collimated before entering the SLIM illumination path, whereas the compact laser-diode modules provided a more spatially uniform propagating beam profile. Fluorescence intensities were adjusted independently for visualization and should not be directly compared across panels. Scale bars, 1,000 μm in the xy projection and 100 μm in the enlarged yz views.

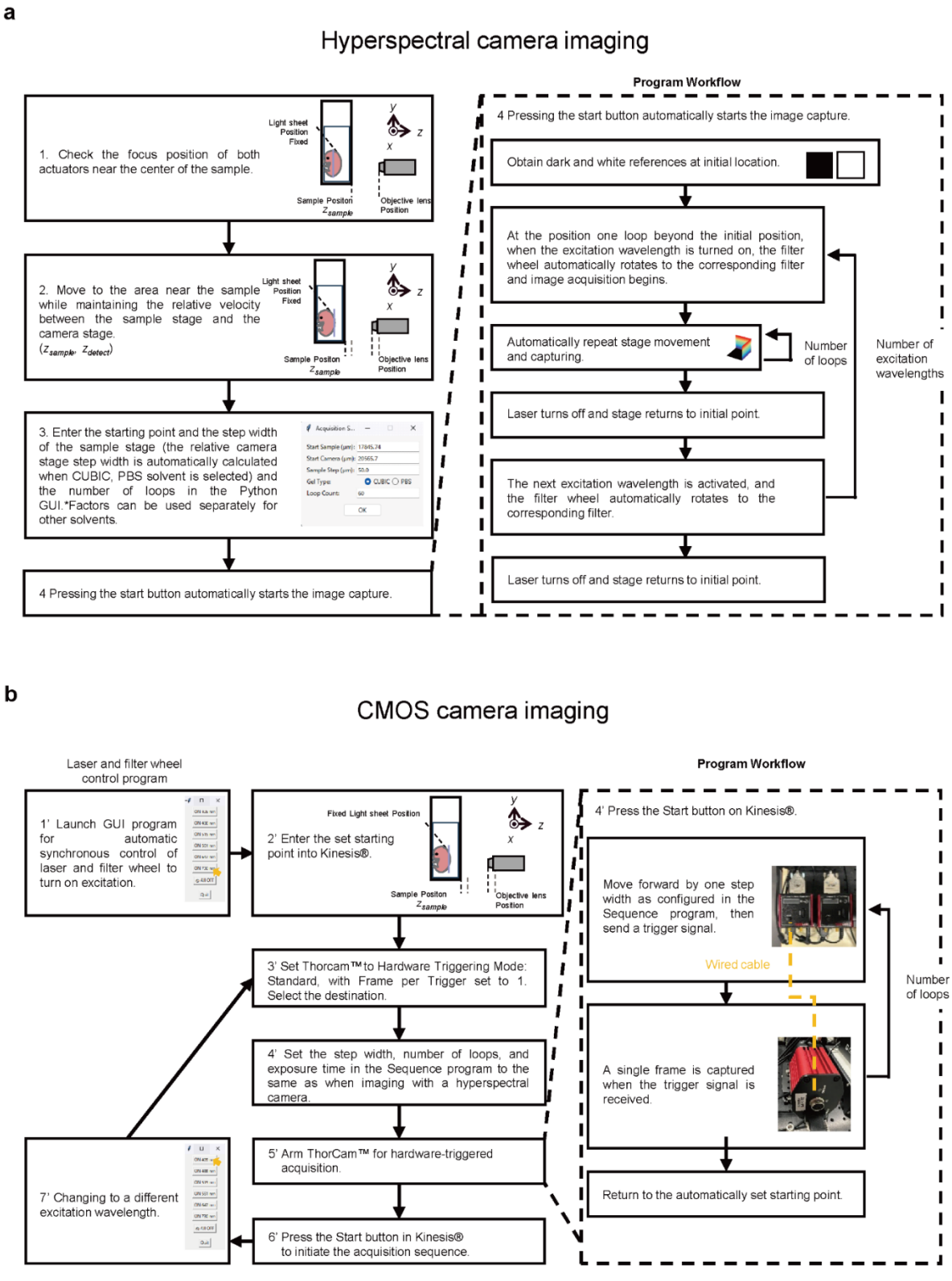

Supplementary Fig. 12 | Imaging workflow of descSPIM-Galaxy.

For channels subjected to linear unmixing, the kinematic cage cube is physically removed

(mirror removed) to allow multi-channel acquisition using the hyperspectral camera. Nuclear staining signals are acquired by both the hyperspectral camera and the CMOS camera, and the resulting datasets are aligned through post hoc image registration based on the nuclear channel (see **Supplementary Fig. 7**). **a,** Workflow of hyperspectral imaging. A custom Python-based GUI enables fully automated 3D hyperspectral imaging across multiple excitation wavelengths. Users specify the starting position, step size, number of loops, and scaling coefficients defining the relative displacement between the sample stage and the detection stage. This automation allows for efficient, reproducible volumetric data acquisition using excitation-multiplexed illumination. **b,** To ensure imaging stability, a custom acquisition program was developed based on Thorlabs Kinesis® and ThorCam™ software. With only the addition of a signal cable, the system enables acquisition of multistack datasets that are compatible with registration to image data obtained from the hyperspectral camera.

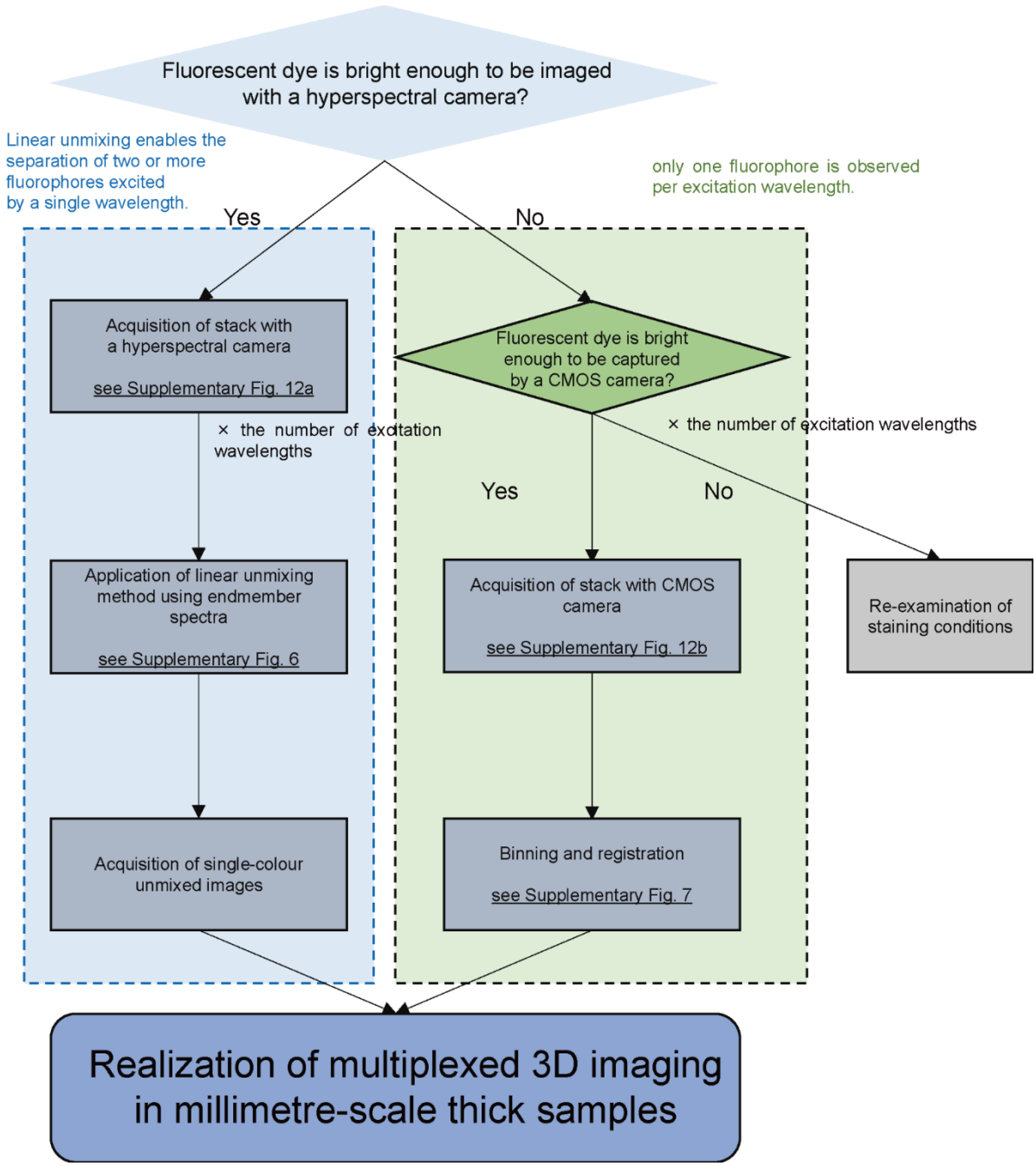

Supplementary Fig. 13 | Comprehensive schematic overview of the imaging and processing pipeline for descSPIM-Galaxy.

Flow chart summarising the descSPIM-Galaxy imaging and processing pipeline. For each fluorophore, emission intensity is first assessed: if sufficient for hyperspectral detection, a multi-excitation z-stack is recorded with the hyperspectral camera (**Supplementary Fig. 12a**), slice-by-slice linear unmixing with end-member spectra is performed (**Supplementary Fig. 6**), and single-color unmixed volumes are produced; if too weak, fluorescence is captured with

the CMOS camera, acquisition time scaling with the number of excitation wavelengths (**Supplementary Fig. 12b**), after which CMOS stacks are binned to the hyperspectral pixel size and registered to the hyperspectral nuclear channel using successive Euclidean, affine and SyN transformations (**Supplementary Fig. 7**). Fluorophores too dim for either route prompt re-evaluation of staining conditions. The resulting hyperspectral and CMOS datasets are then merged, achieving superultra-multicolour three-dimensional imaging of millimetre-scale cleared samples.

Method	Structural / live imaging demonstration	Immersion / medium	Lateral resolution (µm)	Axial resolution (µm)	Cost (USD)	Effective magnification	Camera pixel size (µm)	Image pixel size (µm)	Pixels / image (MP)	Channel number demonstrated	Intended setting
descSPIM-Galaxy	Structural	Air	7.27	27.22	~73,000	1×	5.5	5.5	2.23	11 (beads); 7 (embryo)	Lab
descSPIM-Deepsky	Structural	Air	1.09	4.06–6.40	34,000-64,000	10×	3.45	0.345	8.9	2–3	Lab
descSPIM-Fullmoon	Structural	Air	4.99	43.3	45,000-76,000	1×	3.76	3.76	60	3	Lab
descSPIM-SLIM	Structural	Air	4.42	6.68-11.62	15,000 (3-color LD modules) ~37,000 (4-color fiber-coupled laser)	1×	3.45	3.45	12.3	3–4	Lab / Education
descSPIM-basic	Structural	Air	4.2	7.2-26.0	20,000–50,000	1×	3.45	3.45	8.9	3–4	Lab
UC2	Structural / live	Air	not reported	not reported	~450 USD	varies	varies	varies	varies	1	Education
EduSPIM	Structural	Air	not reported	not reported	not reported	9.1×	not reported	not reported	not reported	1	Education / Museum
mesoSPIM	Structural	Air	2.7	5.57-6.52	170,000–240,000	4× (0.63× – 6.3×)	6.5	1.625	4	1	Facility
Benchtop mesoSPIM	Structural	Air	1.5–2.6	3.3–4.0	100,000–106,000	0.9× –20×	4.25	0.213–0.85	15	2	Facility
OpenSPIM	Structural / live	Water	Varies	Varies	30,000–50,000	Varies	Varies	Varies	Varies	1	Facility
X-OpenSPIM	Live	Water	not reported	not reported	~14,000 USD upgrade (13,000 EUR; without cameras/self-made parts)	40×	6.5	0.1625	5.5	2	Facility
pLSM	Structural / live	Air or oil	0.91–1.74	5.06–6.13	10,000–30,000	10× or 16.7×	3.45	0.207–0.345	8.9	3	Research prototype
HySIL / SCOPE-enabled pLSM	Structural	Hybrid RI ≈1.46; multi-immersion compatible	~0.56–0.75	~5–11	pLSM base 10,000–30,000 USD + SCOPE module	5× or 10×	3.45	0.345	8.9	3 (bead demo)	Research prototype
Isotropic aberration-corrected LSFM	Structural	RI 1.33–1.56 multi-immersion	0.85	0.85	not reported	16× detection lens	6.5	~0.38	4.2	3	Research prototype
Altair-LSFM	Structural / live	Water / aqueous coverslip samples	0.235	0.35	~150,000	50× effective	6.5	0.130	4.2	4 fixed; 2 live	Lab
SHy-Cam LSFM	Live	Water / Danieau solution	not reported	not reported	~6,000 (add-on only)	44×	not reported	not reported	5	6 (beads); 5 (in vivo zebrafish)	Research prototype
Hyperspectral LSFM	Live	Water	not reported	not reported	not reported	13.75×	not reported	not reported	not reported	5 (zebrafish)	Research prototype

Supplementary Table 1 | Specification comparison of descSPIM-Advanced with accessible and recent microscopy systems

Specifications of descSPIM-Advanced configurations developed in this study are compared with previously reported systems, including descSPIM-basic[4], UC2[5], EduSPIM[6], mesoSPIM[7], Benchtop mesoSPIM[8], OpenSPIM[9], X-OpenSPIM[10], pLSM[11], HySIL/SCOPE-enabled pLSM[12], isotropic aberration-corrected LSFM[13], Altair-LSFM[14], Hyperspectral LSFM[15], SHy-Cam LSFM[16]. The table structure was adapted from Supplementary Table 2 of the pLSM report[8] and Table 1 of the Altair-LSFM report[11]. Values are based on published reports and supplementary information where available. “Varies” indicates configuration-dependent values, and “not reported” indicates values not explicitly provided in the original publication.

Supplementary references

1. Lawson, C.L. and Hanson, R.J. (1974) Solving Least Squares Problems. Prentice-Hall, Englewood Cliffs. - References - Scientific Research Publishing. https://www.scirp.org/reference/referencespapers?referenceid=2549470.

2. Avants, B. B., Epstein, C. L., Grossman, M. & Gee, J. C. Symmetric diffeomorphic image registration with cross-correlation: evaluating automated labeling of elderly and neurodegenerative brain. *Med. Image Anal.* **12**, 26–41 (2008).

3. Mano, T. *et al.* CUBIC-Cloud provides an integrative computational framework toward community-driven whole-mouse-brain mapping. *Cell Rep. Methods* **1**, (2021).

4. Otomo, K. *et al.* descSPIM: an affordable and easy-to-build light-sheet microscope optimized for tissue clearing techniques. *Nat. Commun.* **15**, 4941 (2024).

5. Diederich, B. *et al.* A versatile and customizable low-cost 3D-printed open standard for microscopic imaging. *Nat. Commun.* **11**, 5979 (2020).

6. Jahr, W., Schmid, B., Weber, M. & Huisken, J. eduSPIM: Light Sheet Microscopy in the Museum. *PloS One* **11**, e0161402 (2016).

7. Voigt, F. F. *et al.* The mesoSPIM initiative: open-source light-sheet microscopes for imaging cleared tissue. *Nat. Methods* **16**, 1105–1108 (2019).

8. Vladimirov, N. *et al.* Benchtop mesoSPIM: a next-generation open-source light-sheet microscope for cleared samples. *Nat. Commun.* **15**, 2679 (2024).

9. Pitrone, P. G. *et al.* OpenSPIM: an open-access light-sheet microscopy platform. *Nat. Methods* **10**, 598–599 (2013).

10. Girstmair, J., Moon, H., Brillard, C., Haase, R. & Tomancak, P. Time to Upgrade: A New OpenSPIM Guide to Build and Operate Advanced OpenSPIM Configurations. *Adv. Biol.* **6**, e2101182 (2022).

11. Chen, Y. *et al.* Low-cost and scalable projected light-sheet microscopy for the high-resolution imaging of cleared tissue and living samples. *Nat. Biomed. Eng.* **8**, 1109–1123 (2024).

12. Gong, C. *et al.* Hybrid solid−liquid optics enable scalable, high-resolution light-sheet microscopy across diverse immersion media. *Nat. Biotechnol.* 1–13 (2026)

doi:10.1038/s41587-026-03172-7.

13. Aakhte, M. *et al.* Isotropic, aberration-corrected light sheet microscopy for rapid high-resolution imaging of cleared tissue. *Nat. Biotechnol.* 1–11 (2025).

14. Haug, J., Gałecki, S., Lin, H.-Y., Wang, X. & Dean, K. M. A high-resolution, easy-to-build light-sheet microscope for subcellular imaging. *eLife* **14**, RP106910 (2026).

15. Jahr, W., Schmid, B., Schmied, C., Fahrbach, F. O. & Huisken, J. Hyperspectral light sheet microscopy. *Nat. Commun.* **6**, 1–7 (2015).

16. Wang, P. *et al.* A single-shot hyperspectral phasor camera for fast, multi-color fluorescence microscopy. *Cell Rep. Methods* **3**, (2023).